Comparative Studies of Front-End Model Predictive Control for Direct Inductive Power Transfer Systems

Huiwen Xiao, Yun Yang, *Member, IEEE*, Kaiyuan Wang, *Student Member, IEEE*, and Jiayang Wu, *Member, IEEE*

***Abstract*—In this article, two transmitter-side model predictive control (MPC), namely, a model predictive-based phase shift control (MPPC) and a model predictive-based frequency control (MPFC), are proposed for direct inductive power transfer (IPT) systems. Both MPC strategies are empirically verified to have better dynamic responses than the proportional-integral (PI)-based counterparts using inexpensive digital controllers, but the MPFC is proven to be better than the MPPC for direct IPT systems if variable frequency operations are allowed. Both simulation and experimental results confirm that the MPPC will suffer from notching effects and high-order harmonics caused by the dead time of transmitter-side inverters, while the MPFC is immune from the dead time effects. The results also validate that the MPFC with a parallelly proposed initial frequency selection algorithm can cover the shortcomings of the MPPC in achieving soft switching for IPT systems over wide load conditions. Besides, the transmitter-side inverter with MPFC is demonstrated to have lower radiation noise than the same inverter with MPPC in practice.**

***Index Terms*—Dead time, inductive power transfer (IPT), initial frequency selection, model predictive-based frequency control (MPFC), model predictive-based phase shift control (MPPC).**

I. Introduction

TO ALLEVIATE the hassle of wired charging in consumer electronics, power tools, electrified transportation, and medical equipment, inductive power transfer (IPT) technologies have been developed rapidly over the last two decades [1]. A typical example is that the control technologies of IPT are oriented from compatibility to higher efficiency [2], [3], [4], [5], faster dynamic tracking [6], [7], [8], more robust against disturbance [9], [10], [11], better thermal management [12], [13], lower electromagnetic interference (EMI) [14], [15], etc. Nevertheless, the development of wideband gap (WBG) semiconductor devices will further push the boundaries of control technologies to enable IPT systems with higher power and higher frequency operations [16]. A new control paradigm for the next-generation IPT is illustrated in [17] to showcase its huge benefits on receiver manufactures by extensively simplifying the receiver circuits. The core concept of the new control paradigm is to shift all the receiver-side controllers to the transmitter side, such that the main power circuits of the IPT system, auxiliary power supplies of controllers, and protection circuits can be significantly reduced to enhance the overall efficiency of the IPT system, and the reliability, cost-effectiveness, and power density of the receiver. Direct IPT system refers to an IPT system with only active switches at the transmitter side, while the rectifier circuit at the receiver side is passive. Therefore, all the control schemes are designed for the power converters at the transmitter sides, and primary-side control for the transmitter-side inverter becomes crucial for the power flow regulations of direct IPT systems.

Primary-side IPT control is not new, as its early form has been reported in [18]. The output voltage of the studied IPT system with an *LCL* transmitter circuit and an *LC* parallel receiver circuit is regulated by a proportional-integral (PI)-based phase shift control via a low-latency communication from the receiver to the transmitter. Primary-side PI-based frequency control is an alternative to the primary-side PI-based phase shift control. In [19], a center frequency selection algorithm is proposed to control an IPT system with an active rectifier at the receiver side for light-duty electric vehicles. It is more straightforward to regulate the power flow of IPT, with its resemblance to a power transmission network having a reactive power voltage. A typical primary-side frequency control is the self-oscillating control, which requires only simple receiver feedbacks [20], [21], [22]. The advantages of frequency control over phase shift control are more than that. It has been reported that the frequency control is easier to achieve soft switching than the phase shift control for the transmitter-side inverter [14], [15], [24], [25]. For direct IPT systems with light load conditions, the frequency control is able to achieve zero-voltage switching (ZVS), while the phase shift control cannot only if auxiliary circuits are added [26]. Nevertheless, frequency control is not compliant with the standards that require fixed or narrow range operating frequencies [27], [28], [29]. By far, both primary-side phase shift control and primary-side frequency control are extensively investigated in [30], [31], [32], [33], and [34], while most of them are PI-based and a few of them are designed based on direct IPT systems.

Manuscript received 12 April 2023; revised 14 June 2023; accepted 16 July 2023. Date of publication 19 July 2023; date of current version 1 September 2023. This work was supported in part by NTU Start Up under Grant 03INS001563C140 and in part by the Ministry of Education (MoE) Academic Research Fund (AcRF) Tier-1 under Grant RG116/21. Recommended for publication by Associate Editor M. Liu. *(Corresponding author: Yun Yang.)*

Huiwen Xiao is with the Hong Kong Polytechnic University, Hong Kong, SAR, China (e-mail: xiaohuiwen1223@gmail.com).

Yun Yang, Kaiyuan Wang, and Jiayang Wu are with the Nanyang Technological University, Singapore 639798 (e-mail: yun.yang@ntu.edu.sg; KAIYUAN002@e.ntu.edu.sg; jiayang.wu@ntu.edu.sg).

Color versions of one or more figures in this article are available at https://doi.org/10.1109/TPEL.2023.3296729.

Digital Object Identifier 10.1109/TPEL.2023.3296729

To bridge the research gaps, a model predictive-based phase shift control (MPPC) and a model predictive-based frequency control (MPFC) are proposed and compared in this article. Finite-control-set model predictive control (FCS-MPC) is a well-established time-sequence control that exhibits superior dynamic responses and robustness against disturbance compared to conventional PI-based control for power electronics systems [35], [36], [37], [38]. FCS-MPC with one-step or two-step predictions is widely adopted to regulate the output voltages of dynamic IPT systems [39], [40], [41]. However, FCS-MPC for direct IPT systems has not been studied yet. The proposed MPPC and MPFC are typical FCS-MPC with one-step prediction. Both MPC are established based on the canonical system models and practical factors, including dead time, turn-ON delay time, turn-OFF delay time, and parasitic capacitances of the transmitter-side inverters, bifurcation phenomenon of IPT systems, and determination of initial switching frequencies. Compared to the PI-based counterparts, the MPPC and MPFC can perform superior dynamic responses, such as smaller overshoots and shorter settling time. However, the MPPC is vulnerable to the notching effects and current distortion being caused by the dead time. It is also ineffective in achieving soft switching for IPT systems with light load conditions. On the contrary, the MPFC is not affected by the dead time effects and the soft switching of transmitter-side inverters can be guaranteed over a wide load range. As a result, the radiation noises of transmitter-side inverters controlled by the MPFC are lower than those of the MPPC. The accuracy of MPFC will be affected by the inherent frequency bifurcation nature of IPT systems. To prevent this potential issue, a new frequency selection algorithm is presented to find out the optimal initial switching frequency of the transmitter-side inverter. The optimal initial frequency can basically ensure the ZVS of the inverter. Thus, the proposed MPFC is better than MPPC for direct IPT systems if fixed frequency operations are not rigidly required. The main contributions of this article can be summarized as follows.

1) This might be the first article to present and compare two FCS-MPC, i.e., MPPC and MPFC, for transmitter-side inverters of direct IPT systems. Both simulation and experimental result validate that both MPC have superior dynamic performance than their PI-based counterparts, and MPFC is better than MPPC if the IPT system can operate with variable frequencies.
2) The effects of dead time on MPPC and MPFC for direct IPT systems are evaluated by analyzes, simulation, and empirical results for the first time.
3) A new frequency selection algorithm is proposed to enhance the accuracy of MPFC by resolving the initial frequency issue caused by inherent frequency bifurcation nature of IPT systems.
4) The MPFC is practically verified to have less radiation noise than the MPPC for transmitter-side inverters of IPT systems.

II. Basic Analyzes of the Proposed MPFC and MPPC

To simplify the analysis without losing generality, a direct series–series (SS)-compensated IPT system is analyzed in this article. The circuit diagram of a typical direct SS-compensated IPT system is plotted as shown in Fig. 1. Here, $V_{\rm in}$ is the input dc voltage. $v_{\rm p}$ and $v_{\rm s}$ are the input and output voltages of the transmitter and receiver resonators. $i_{\rm p}$ and $i_{\rm s}$ are the transmitter and receiver currents. $i_{\rm rec}$ and $i_{\rm co}$ are the rectified current and filter capacitor current. $I_{\rm o}$ and $U_{\rm o}$ are the output current and voltage. $L_{\rm p}$ and $L_{\rm s}$ are the self-inductances of transmitter and receiver coils. M is the mutual inductance between the coupled coils. $C_{\rm p}$ and $C_{\rm s}$ are the compensation capacitances to satisfy $\omega_{\rm o} = 1/\sqrt{L_{\rm p}C_{\rm p}} = 1/\sqrt{L_{\rm s}C_{\rm s}}$, where $\omega_{\rm o}$ is the resonant frequency. $R_{\rm p}$ and $R_{\rm s}$ are the equivalent series resistances (ESRs) of the resonators. $C_{\rm o}$ is the filter capacitance. $R_{\rm L}$ is the load resistance.

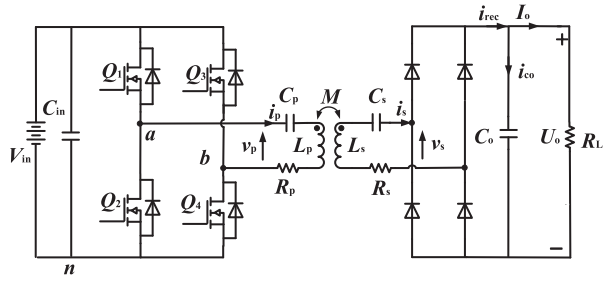

Fig. 1. Schematic circuit diagram of a typical SS-compensated IPT system.

According to the Fourier analysis, the fundamental components of $v_{\rm p}$ and $i_{\rm s}$ can be obtained as

$$v_{\rm p1}(t) = \frac{4V_{\rm in}\cos\left(\frac{\alpha}{2}\right)}{\pi}\sin(\omega_{\rm s}t) \tag{1}$$

$$i_{\rm s1}(t) = \frac{4V_{\rm in}\omega_{\rm s}M\cos\left(\frac{\alpha}{2}\right)}{\pi\left|Z_{\rm p}Z_{\rm s}+\omega_{\rm s}^2M^2\right|}\sin\left(\omega_{\rm s}t+\frac{\pi}{2}+\theta\right) \tag{2}$$

where the transmitter and receiver impedances are

$$\begin{cases} Z_{\rm p} = j\omega_{\rm s}L_{\rm p} + \frac{1}{j\omega_{\rm s}C_{\rm p}} + R_{\rm p} \\ Z_{\rm s} = j\omega_{\rm s}L_{\rm s} + \frac{1}{j\omega_{\rm s}C_{\rm s}} + R_{\rm s} + R_{\rm eqL} \end{cases}. \tag{3}$$

Here, α is the phase shift angle of the diagonal power switches of the transmitter-side inverter (i.e., Q_1 and Q_4, Q_2 and Q_3). It is worth noting that α is controlled at 0° when the proposed MPFC is adopted for the IPT system. $R_{\rm eqL}$ is the equivalent load resistance of the diode-bridge rectifier, filter capacitor, and resistive load. For general load conditions [42], $R_{\rm eqL}$ and $R_{\rm L}$ are in linear relationship (i.e., $R_{\rm eqL} = 8R_{\rm L}/\pi^2$). θ is the phase angle of the term $Z_{\rm p}Z_{\rm s} + {\omega_{\rm s}}^2M^2$, while the magnitude of $Z_{\rm p}Z_{\rm s} + {\omega_{\rm s}}^2M^2$ (i.e., $|Z_{\rm p}\ Z_{\rm s} + {\omega_{\rm s}}^2M^2|$) is constant in one cycle. When the proposed MPPC is adopted for the IPT system, the switching angular frequency (i.e., $\omega_{\rm s}$) is controlled at $\omega_{\rm o}$, the impedances $Z_{\rm p}$ and $Z_{\rm s}$ are simplified as $R_{\rm p}$ and $R_{\rm s} + R_{\rm eqL}$, and θ is zero.

Based on (2), the average output current of the diode bridge rectifier can be calculated as

$$\langle i_{\rm rec}(t)\rangle_{T_{\rm s}} \cong \frac{1}{T_{\rm s}}\int_0^{T_{\rm s}}|i_{\rm s1}(t)|\,dt = \frac{16V_{\rm in}Mf_{\rm s}\cos\left(\frac{\alpha}{2}\right)}{\pi\left|Z_{\rm p}Z_{\rm s}+\omega_{\rm s}^2M^2\right|} \tag{4}$$

where $f_{\rm s}$ is the switching frequency and $T_{\rm s}$ is the sampling period. The filter capacitor current $i_{\rm co}$ can be expressed as

$$i_{\rm co}(t) = \langle i_{\rm rec}(t)\rangle_{T_{\rm s}} - \langle I_{\rm o}(t)\rangle_{T_{\rm s}} = C_{\rm o}\frac{d\left(\langle I_{\rm o}(t)\rangle_{T_{\rm s}}R_{\rm L}\right)}{dt}. \tag{5}$$

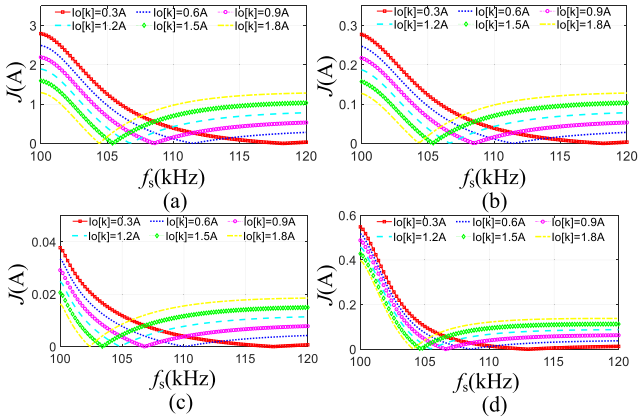

Fig. 2. J-f_s curves of the IPT system with (a) $M = 6.243$ μH, $R_L = 0.1\Omega$, (b) $M = 6.243$ μH, $R_L = 1\Omega$, (c) $M = 6.243$ μH, $R_L = 7\Omega$, and (d) $M = 3.243$ μH, $R_L = 1\Omega$.

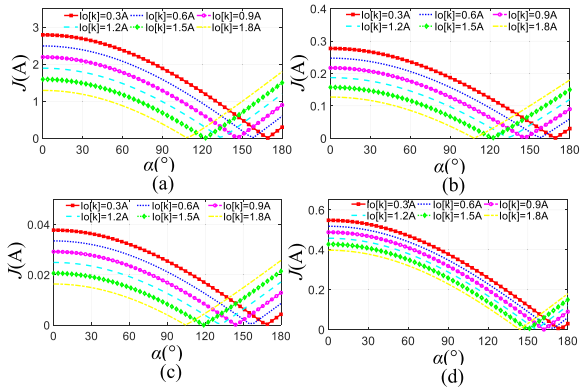

Fig. 3. J-α curves of the IPT system with (a) $M = 6.243$ μH, $R_L = 0.1\Omega$, (b) $M = 6.243$ μH, $R_L = 1\Omega$, (c) $M = 6.243$ μH, $R_L = 7\Omega$, and (d) $M = 3.243$ μH, $R_L = 1\Omega$.

By applying Euler's forward discretization for (4), the output current at the next sampling time $I_o[k+1]$ can be estimated based on the output current at the current sampling time $I_o[k]$ as

$$I_o[k+1] = \frac{16V_{in}M\cos\left(\frac{\alpha}{2}\right)}{C_oR_L\pi\left|Z_pZ_s+\omega_s^2M^2\right|} + \left(1-\frac{1}{C_oR_Lf_s}\right)I_o[k]. \tag{6}$$

Apparently, the output current can be regulated by f_s and α. The proposed MPFC and MPPC are designed for controlling f_s and α, respectively. For both MPC, $I_o[k+1]$ is regulated to track the reference I_{ref} using the canonical cost function

$$\min J = |I_{ref} - I_o[k+1]| \tag{7.1}$$

$$\text{s.t. } 0 \le I_{ref} \le I_{refmax} \tag{7.2}$$

$$f_{smin} \le f_s \le f_{smax}. \tag{7.3}$$

The output current reference and the switching frequency of the system are strictly constrained within the boundaries (7.2) and (7.3). The current constraints are set for ensuring the system stability, while the frequency constraints are set based on hardware limits.

For the MPFC, α is controlled to be zero. At the sampling time k, the output currents $I_o[k+1]$ are predicted based on f_s, $f_s+\Delta f$, and $f_s-\Delta f$, where Δf is the step change of the switching frequency. By comparing the three cost functions, the frequency with the minimum values is adopted as the switching frequency for the transmitter-side inverter at the sampling time $k+1$. It is worth noting that the step change Δf can be fixed or variable. In this article, fixed Δf is adopted for fair comparisons. For variable Δf, small Δf can be used at steady states for ensuring accurate tracking and large Δf can be used at transient states for fast dynamic responses. The curves portraying the relationships between the cost functions J and f_s for different output current references, load conditions, and mutual inductances are depicted, as shown in Fig. 2. Apparently, optimal f_s, which corresponds to minimum J, can be found for all the operating conditions.

For the proposed MPPC, following the conventional phase shift control [14], [27], [30], [31], f_s is fixed at the resonant frequency. The output current $I_o[k+1]$ is monotonically changed with the phase shift angle α. Thus, by increasing or decreasing α with the step change $\Delta\alpha$, the predicted output current will increase or decrease accordingly. Similar to the MPFC, fixed or variable $\Delta\alpha$ can be adopted. In this article, only fixed $\Delta\alpha$ is investigated for fair comparisons. Adaptive phase shift control has been studied in [43]. By comparing the cost functions of α, $\alpha+\Delta\alpha$, and $\alpha-\Delta\alpha$, the phase shift angle corresponding to the minimum cost function is adopted for the transmitter-side inverter at the sampling time $k+1$. The α-J curves for different operating conditions are plotted, as shown in Fig. 3. Obviously, optimal α (i.e., α_{opt}), which corresponds to minimum J, also exists for all the operating conditions.

III. Effects of Main Parasitic Parameters of the Transmitter-Inverter on the MPC

A. Effects on MPPC

To analyze the effects of main parasitic parameters of the transmitter-inverter on MPPC, the operation states of the inverter in one cycle are studied based on the schematic waveforms of major parameters in Fig. 4. $Q_1{}^*$ and $Q_4{}^*$ denote ideal gate pulses without dead time, while Q_1, Q_2, Q_3, and Q_4 indicate nonideal gate pulses with dead time. $v_{an}{}^*$ and $v_{bn}{}^*$ are ideal phase-leg voltages. $v_p{}^*$ denotes the ideal square-wave voltage between the phase a and phase b legs. v_{an} and v_{bn} are nonideal phase-leg voltages. v_p denotes the nonideal square-wave voltage between the phase a and phase b legs. T_d, T_{ond}, and T_{offd} are dead time, turn-ON delay time, and turn-OFF delay time. φ_{Td} is the dead time angle (i.e., $\varphi_{Td} = \omega_sT_d$). The existence of dead time will cause notching effects [44]. By considering T_{ond} and T_{offd}, the cutoff angles of the notching effects will be extended to $\varphi_{Td+Tond-Toffd}$ (i.e., $\varphi_{Td+Tond-Toffd} = \omega_s(T_d+T_{ond}-T_{offd})$). It is worth noting that the cut-off angles will change if the phase angle between v_{p1} and i_p (i.e., φ) and the phase angle between v_{p1} and v_p (i.e., φ_y) are changed. U_{sat} and U_{diode} are the forward voltages of switching components and body diodes.

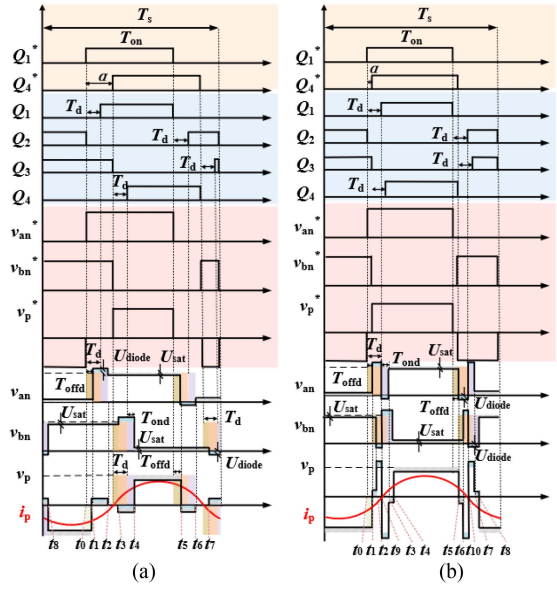

Fig. 4. Main waveforms of the transmitter-side inverter controlled by MPPC with (a) $\alpha > \varphi_{Td+\,Tond-\,Toffd}$ and (b) $\alpha < \varphi_{Td+\,Tond-\,Toffd}$.

The operation states of the inverter with $\alpha > \varphi_{Td+\,Tond-\,Toffd}$ [as shown in Fig. 4(a)] are discussed in the following.

1) *Stage 1 (from t_0 to t_1):* $Q_1{}^*$ is turned ON, while Q_1 remains turn-OFF state. Q_2 is not turned OFF immediately, while Q_3 remains turn-ON state. Hence, i_p flows through Q_2 and Q_3. The phase voltage v_{an} is increased by U_{sat}, while the phase voltage v_{bn} is decreased by U_{sat}. Thus, the phase voltage difference v_p is reduced by $2U_{sat}$.
2) *Stage 2 (from t_1 to t_2):* Q_2 is turned OFF, while Q_3 remains turn-ON state. Therefore, i_p flows through D_1 and Q_3. The phase voltage v_{an} is increased by U_{diode}, while the phase voltage v_{bn} is decreased by U_{sat}. Thus, the phase voltage difference v_p is increased by $U_{sat}+U_{diode}$.
3) *Stage 3 (from t_2 to t_3):* i_p changes from negative to positive, Q_1 is turned ON, while Q_3 remains turn-ON state. i_p flows through Q_1 and Q_3. Both the phase voltage v_{an} and v_{bn} is reduced by U_{sat}. During this period, the phase voltage difference v_p is zero.
4) *Stage 4 (from t_3 to t_4):* Q_1 remains turn-ON state, while Q_3 is turned OFF and i_p flows through Q_1 and D_3. The phase voltage v_{an} is reduced by U_{sat}, while the phase voltage v_{bn} is increased by U_{diode}. Thus, the phase voltage difference v_p is increased by $U_{sat}+U_{diode}$.
5) *Stage 5 (from t_4 to t_5):* Q_4 is turned ON, while Q_1 remains turn-ON state. i_p flows through Q_1 and Q_4. The phase voltage v_{an} is reduced by U_{sat}, while the phase voltage v_{bn} is increased by U_{sat}. Hence, v_p is reduced by $2U_{sat}$.
6) *Stage 6 (from t_5 to t_6):* Q_1 is turned OFF, while Q_4 remains turn-ON state. i_p flows through D_2 and Q_4. The phase voltage v_{an} is increased by U_{diode}, while the phase voltage v_{bn} is increased by U_{sat}. Therefore, v_p is increased by $U_{diode}+U_{sat}$.
7) *Stage 7 (from t_6 to t_7):* i_p is changed from positive to negative, Q_2 is turned ON, while Q_4 remains the turn-ON state. i_p flows through Q_2 and Q_4. Both the phase voltages v_{an} and v_{bn} are increased by U_{sat}. During this period, the phase voltage difference v_p is zero.
8) *Stage 8 (from t_7 to t_8):* Q_4 is turned OFF, while Q_2 remains turn-ON state, and i_p flows through Q_2 and D_4. v_{an} is increased by U_{sat}, while the phase voltage v_{bn} is increased by U_{diode}. Thus, the phase voltage difference v_p is increased by $U_{sat}+U_{diode}$.
9) *Stage 9 (from t_8 to t_0):* Q_3 is turned ON and Q_2 remains the turn-ON state. i_p is negative and flows through Q_2 and Q_3. The changes of v_{an}, v_{bn}, and v_p are consistent with those in the Stage 1.

For $\alpha < \varphi_{Td+\,Tond-\,Toffd}$, the Stage 3 will be replaced by the following Stage 10 and Stage 11, and the Stage 7 will be altered by the Stage 12 and Stage 13, while the remaining operation stages are the same [as shown in Fig. 4(b)].

1) *Stage 10 (from t_2 to t_9):* Q_3 is turned OFF, and i_p is negative and flows through D_1 and D_4. The phase voltage v_{an} is increased by U_{diode}, while the phase voltage v_{bn} is increased by U_{diode}. Thus, the phase voltage difference v_p is increased by $2U_{diode}$.
2) *Stage 11 (from t_9 to t_3):* i_p changes from negative to positive, and flows through D_2 and D_3. The phase voltage v_{an} is increased by U_{diode}, while the phase voltage v_{bn} is increased by U_{diode}. Thus, the phase voltage difference v_p is increased by $2U_{diode}$.
3) *Stage 12 (from t_6 to t_{10}):* Q_4 is turned OFF, and i_p is positive and flows through D_2 and D_3. The phase voltage v_{an} is increased by U_{diode}, while the phase voltage v_{bn} is increased by U_{diode}. Thus, the phase voltage difference v_p is increased by $2U_{diode}$.
4) *Stage 13 (from t_{10} to t_7):* i_p changes from positive to negative, and flows through D_1 and D_4. The phase voltage v_{an} is increased by U_{diode}, while the phase voltage v_{bn} is increased by U_{diode}. Thus, the phase voltage difference v_p is increased by $2U_{diode}$.

By comparing the waveforms of $v_p{}^*$ and v_p in Fig. 4, the period of positive v_p is dwindled when T_d, T_{ond}, T_{offd} are considered. For an ideal system with the proposed MPPC, the phase shift angle α and sensitivities of I_o with respect to α can be derived based on (6) as

$$\alpha = 2\arccos\left(\frac{I_o[k]\pi\left|Z_pZ_s+\omega_s^2M^2\right|}{16V_{in}Mf_s}\right) \tag{8}$$

and

$$\left|\frac{\partial I_o[k]}{\partial\alpha}\right| = \frac{8V_{in}f_s}{\pi\left|\frac{R_p\left(R_s+R_{eqL}\right)}{M}+\omega_s^2M\right|}\sin\left(\frac{\alpha}{2}\right). \tag{9}$$

Apparently, α approaches zero for heavy load conditions when V_{in} is decreased and R_L is increased. For light load conditions, α are nonzero. Besides, deviations of α will induce output current offsets. Due to the existence of T_d, T_{ond}, and T_{offd}, the calculated α based on (8) is different from the actual α. As a result, the output range will be narrower. Even if $\alpha < \varphi_{Td+\,Tond-\,Toffd}$, the notching effects of v_p are unavoidable. To indicate the effects of parasitic parameters on the MPC more explicitly, the absolution voltage difference between v_p and $v_p{}^*$

in the positive cycle, namely the voltage loss $\Delta v_{\rm p}$ is calculated. A larger $\Delta v_{\rm p}$ indicates a more serious effect, since the discrepancy between the ideal and actual voltages is larger. For the MPPC, the average $v_{\rm p}{}^*$ in the positive half cycle is

$$v_{\rm p}^* = \frac{\pi - \alpha}{\pi} V_{\rm in}. \tag{10}$$

The average $v_{\rm p}$ in the positive half cycle is

$$v_{\rm p} = \left(\frac{\pi - \alpha}{\pi} - \frac{2\left(T_{\rm d} + T_{\rm ond} - T_{\rm offd}\right)}{T_{\rm s}}\right)\left(V_{\rm in} - 2U_{\rm sat}\right) \tag{11}$$

Then, the voltage loss $\Delta v_{\rm p}$ is

$$\Delta v_{\rm p} = \left(\frac{4\left(T_{\rm d} + T_{\rm ond} - T_{\rm offd}\right)}{T_{\rm s}} - \frac{2\pi - 2\alpha}{\pi}\right) U_{\rm sat} - \frac{2\left(T_{\rm d} + T_{\rm ond} - T_{\rm offd}\right)}{T_{\rm s}} V_{\rm in}. \tag{12}$$

Obviously, $\Delta v_{\rm p}$ is affected by $V_{\rm in}$, $T_{\rm d}$, $T_{\rm ond}$, $T_{\rm offd}$, $U_{\rm sat}$, and α. $T_{\rm ond}$, $T_{\rm offd}$, and $U_{\rm sat}$ are mainly determined by the types of gate driving circuits and switching devices, while $T_{\rm d}$ and α can be controlled by software methods. For active switches with negligible $U_{\rm sat}$, the voltage loss in (12) can be simplified as

$$\Delta\, v_{\rm p} = \frac{2\left(T_{\rm d} + T_{\rm ond} - T_{\rm offd}\right)}{T_{\rm s}} V_{\rm in}. \tag{13}$$

Apparently, the dead time, turn-ON delay time, and turn-OFF delay time will affect the MPPC regulations. Besides, according to (9), the sensitivities of $I_{\rm o}$ with respect to α decrease monotonically for all the operating conditions, which means the $I_{\rm o}$ regulations are less vulnerable against disturbance on α when it approaches zero. For a fixed α, the sensitivities will decrease when $R_{\rm L}$ is increased, $V_{\rm in}$ is decreased, or M is increased ($M > \sqrt{\frac{R_{\rm p}(R_{\rm s}+R_{\rm eqL})}{\omega_{\rm s}^2}}$ in general). Therefore, the MPPC can exhibit more robust output regulation performance for an IPT system with a smaller input voltage, a stronger mutual coupling, and a heavier load condition.

Moreover, it is well-known that the parasitic capacitors of the active switches can result in hard switching for IPT systems with light load conditions [26]. Hence, it is also necessary to compensate the dead time in the MPPC or adding auxiliary circuits to ensure soft switching of the transmitter-side inverter.

B. Effects on MPFC

For MPFC, the transmitter-side inverter can operate in nine states. The main waveforms are shown in Fig. 5.

For $\varphi > (\varphi_{Td+}\, T_{ond-}\, T_{offd})/2$, as shown in Fig. 5(a).

1) *Stage 1 (from t_0 to t_1):* $Q_1{}^*$ is turned ON, while Q_1 remains turn-OFF state. Q_2 and Q_3 are not turned OFF immediately. Hence, $i_{\rm p}$ flows through Q_2 and Q_3. The phase voltage $v_{\rm an}$ is increased by $U_{\rm sat}$, while the phase voltage $v_{\rm bn}$ is decreased by $U_{\rm sat}$. Thus, the phase voltage difference $v_{\rm p}$ is reduced by $2U_{\rm sat}$.
2) *Stage 2 (from t_1 to t_2):* Q_2 and Q_3 are turned OFF. $i_{\rm p}$ flows through D_1 and D_4. The phase voltage $v_{\rm an}$ is increased by $U_{\rm diode}$, while the phase voltage $v_{\rm bn}$ is increased by $U_{\rm diode}$, which results in a $2U_{\rm diode}$ increment of $v_{\rm p}$.

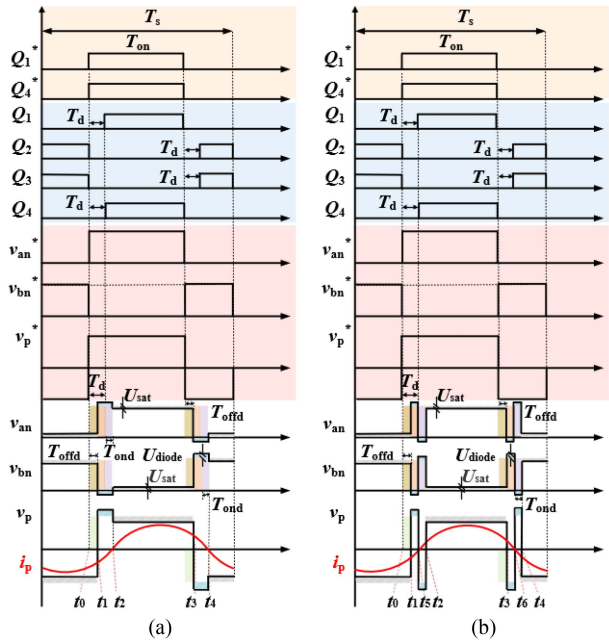

Fig. 5. Main waveforms of the transmitter-side inverter controlled by MPFC with (a) $\varphi > (\varphi_{Td+}\, T_{ond-}\, T_{offd})/2$ and (b) $\varphi < (\varphi_{Td+}\, T_{ond-}\, T_{offd})/2$.

3) *Stage 3 (from t_2 to t_3):* Q_1 and Q_4 are turned ON. $i_{\rm p}$ flows through Q_1 and Q_4. The phase voltage $v_{\rm an}$ is decreased by $U_{\rm sat}$, while the phase voltage $v_{\rm bn}$ is increased by $U_{\rm sat}$. Consequently, $v_{\rm p}$ is reduced by $2U_{\rm sat}$.
4) *Stage 4 (from t_3 to t_4):* Q_1 and Q_4 are turned OFF. $i_{\rm p}$ flows through D_2 and D_3. The phase voltage $v_{\rm an}$ is increased by $U_{\rm diode}$, while the phase voltage $v_{\rm bn}$ is increased by $U_{\rm diode}$. Hence, $v_{\rm p}$ is increased by $2U_{\rm diode}$.
5) *Stage 5 (from t_4 to t_0/):* Q_2 and Q_3 are turned ON. $i_{\rm p}$ flows through Q_2 and Q_3. The changes of $v_{\rm an}$, $v_{\rm bn}$, and $v_{\rm p}$ are the same as those in the Stage 1.

For $\varphi < (\varphi_{Td+}\, T_{ond-}\, T_{offd})/2$, as shown in Fig. 5(b), the Stage 2 is changed by the Stage 6 and Stage 7, while and the Stage 4 is changed by the Stage 8 and Stage 9.

1) *Stage 6 (from t_1 to t_2):* The changes of $v_{\rm an}$, $v_{\rm bn}$, and $v_{\rm p}$ are consistent with those in the Stage 2.
2) *Stage 7 (from t_5 to t_2):* $i_{\rm p}$ changes from negative to positive, and flows through D_2 and D_3. The phase voltage $v_{\rm an}$ is increased by $U_{\rm diode}$, while the phase voltage $v_{\rm bn}$ is increased by $U_{\rm diode}$. Hence, $v_{\rm p}$ is increased by $2U_{\rm diode}$.
3) *Stage 8 (from t_5 to t_2):* The changes of $v_{\rm an}$, $v_{\rm bn}$, and $v_{\rm p}$ are consistent with those in the Stage 4.
4) *Stage 9 (from t_6 to t_4):* $i_{\rm p}$ changes from positive to negative, and flows through D_1 and D_4. The phase voltage $v_{\rm an}$ is increased by $U_{\rm diode}$, while the phase voltage $v_{\rm bn}$ is increased by $U_{\rm diode}$. Hence, $v_{\rm p}$ is increased by $2U_{\rm diode}$.

By comparing the schematic waveforms of $v_{\rm p}{}^*$ and $v_{\rm p}$ in Fig. 5(a), it is intuitive to find out that the periods of positive $v_{\rm p}$ and $v_{\rm p}{}^*$ are the same even if $T_{\rm d}$, $T_{\rm ond}$, and $T_{\rm offd}$ are considered. It is worth noting that the period of positive $v_{\rm p}$ and voltage loss $\Delta v_{\rm p}$ in Fig. 5(b) are similar to those in Fig. 4(b), and the operating frequency is larger than the resonant frequency. Thus,

TABLE I
MAIN DIFFERENCES OF PARASITIC PARAMETER EFFECTS BETWEEN MPPC AND MPFC

Characteristics	MPPC	MPFC
period of positive v_p as compared to that of v_p^*	smaller	same
main effects on the voltage loss Δv_p	T_d, T_{ond}, T_{offd}, α, V_{in}	T_d, T_{ond}, T_{offd}
cut-off angle of notching effects	random	constant
soft switching	need compensation	no change

only the voltage loss in Fig. 5(a) is analyzed. The average v_p^* in the positive half cycle of MPFC is V_{in}, while the average v_p in the positive half cycle is

$$v_p = V_{in} - 2U_{sat} + \frac{4\left(T_d + T_{ond} - T_{offd}\right)}{T_s}\left(U_{sat} + U_{diode}\right). \tag{14}$$

The voltage loss Δv_p can be calculated as

$$\Delta v_p = -\left(2 - \frac{4\left(T_d + T_{ond} - T_{offd}\right)}{T_s}\right) U_{sat} + \frac{4\left(T_d + T_{ond} - T_{offd}\right)}{T_s} U_{diode}. \tag{15}$$

It can be observed from (15) that the voltage loss is related to T_d, T_{ond}, T_{offd}, U_{sat}, and U_{diode}. For specific gate driving circuits and active switches, T_{ond}, T_{offd}, U_{diode}, and U_{sat} are determined. The only controllable parameter is T_d. If U_{sat} and U_{diode} are negligible, the voltage loss Δv_p is zero, which means the effects of dead time, turn-ON delay time, and turn-OFF delay time on MPFC regulations are very small. Besides, soft switching of the transmitter inverter with MPFC is easier to be achieved by controlling ω_s to be greater than ω_o [14], [45]. The main differences in the parasitic parameter effects between MPPC and MPFC are summarized in Table I. Clearly, the effects of the main parasitic parameters of the transmitter-inverter on MPFC are less serious than those of MPPC.

IV. FREQUENCY BIFURCATION PHENOMENON OF MPFC

Although MPFC is analyzed to be more robust against parasitic effects than MPPC, the bifurcation issue may result in instability of the system. Based on the equivalent circuit in the frequency domain, the IPT resonators can be described using

$$\begin{bmatrix} \dot{V}_p \\ 0 \end{bmatrix} = \begin{bmatrix} Z_p & -j\omega_s M \\ -j\omega_s M & Z_s \end{bmatrix} \begin{bmatrix} \dot{I}_p \\ \dot{I}_s \end{bmatrix} \tag{16}$$

where $\dot{V}_p$ and $\dot{I}_p$ are the fundamental input voltage and current phasor of the transmitter. $\dot{I}_s$ is the receiver current phasor.

Based on (16), the transconductance and input impedance of the IPT system can be derived as

$$g_m = \frac{\dot{I}_s}{\dot{V}_p} = \frac{j\omega_s M}{Z_p Z_s + \omega_s^2 M^2} \tag{17}$$

$$Z_{in} = \frac{\dot{V}_p}{\dot{I}_p} = Z_p + \frac{\omega_s^2 M^2}{Z_s}. \tag{18}$$

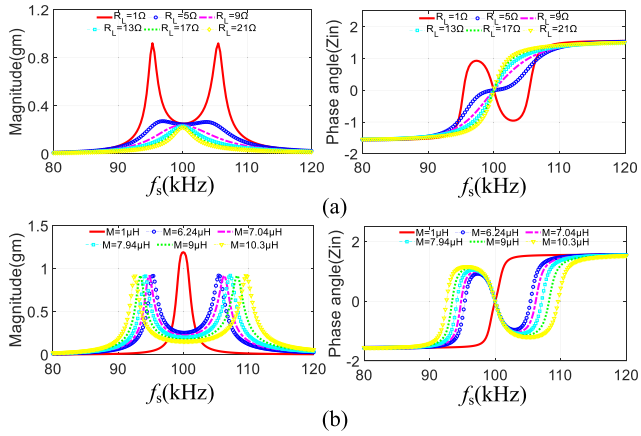

Fig. 6. Spectrums of magnitudes of g_m and phase angles of Z_{in} for the IPT system with (a) $M = 6.243$ μH and (b) $R_L = 1$ Ω.

TABLE II
MAIN PARAMETER VALUES OF THE IPT SYSTEM

Parameter	Value	Parameter	Value	Parameter	Value
L_p	60.9 μH	C_p	41.59 nF	R_p	0.14 Ω
L_s	60.9 μH	C_s	41.59 nF	R_s	0.14 Ω
M	1 to 10.3 μH	C_o	100 μF	R_L	1 to 21 Ω
f_s	80 to 120 kHz	V_{in}	10 V		

Fig. 6 shows the spectrums of magnitudes of g_m and phase angles of Z_{in} for the IPT system with different R_L and M, while other parameter values are given in Table II. The nominal M and R_L are 6.243 μH and 1 Ω, respectively. The resonant frequency is 100 kHz. It can be observed from Fig. 6 that the bifurcation phenomenon (more than one extreme) occurs for many mutual and load conditions, and additional frequencies except the resonant frequency can achieve zero phase angles. In fact, this phenomenon is more serious as the load resistance decreases or the mutual inductance increases. As can be seen in Fig. 6(a), the magnitude extremes of g_m are increased from one to two when R_L is decreased from 21 to 1 Ω. The number of zero-crossing points of Z_{in} is changed from one to three when M is increased from 1 to 10.3 μH. According to (7.1), the objective function of MPFC is to minimize the difference between the predicted output current and the reference current, thus, the IPT system will fail to converge at the optimal frequency and may cause undesirable overshoots during the start-up stage due to nonmonotonicity caused by the frequency bifurcation. Hence, it is harder for the MPFC to converge at optimal operating conditions for dynamic IPT systems. To address this critical issue, the initial frequency of MPFC (i.e., f_{sini}) needs to be properly designed.

V. DETAILS OF MPC DESIGNS

The control block diagram of MPPC is depicted as shown in Fig. 7(a). The output current at the next sampling time $k+1$ is predicted using (6) based on the calculated phase shift angle $\alpha[k+1]$ and measured output current $I_o[k]$. The estimated output current is controlled to track the reference I_{ref} based on the

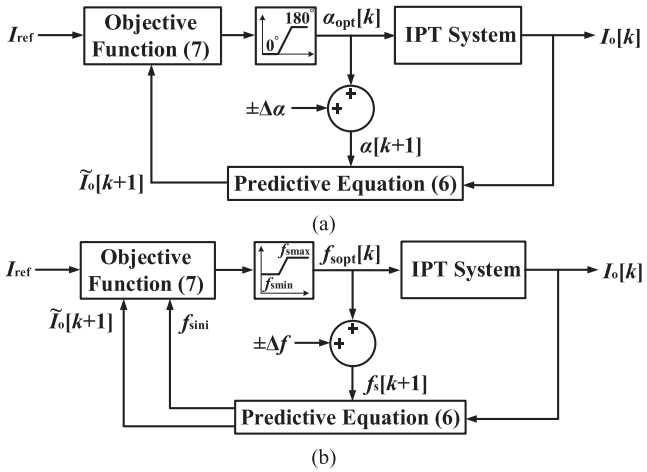

Fig. 7. Control block diagrams of the proposed (a) MPPC and (b) MPFC for IPT systems.

objective function and the constraints in (7). The control output is the optimal phase shift control $\alpha_{\rm opt}$, which is strictly constrained within 0° and 180°. The optimal phase shift angle is adopted for the transmitter-inverter of the IPT system, and incremented or reduced by a step change $\Delta\alpha$ for $\alpha[k+1]$.

For MPFC, the control block diagram is plotted as shown in Fig. 7(b). The output current at the next sampling time $k+1$ is predicted using (6) based on the calculated switching frequency $f_{\rm s}[k+1]$ and measured output current $I_{\rm o}[k]$. Similar to the MPPC, the estimated output current is controlled to track the reference based on (7). However, the control output is the optimal frequency $f_{\rm sopt}$, which is limited by the lower bound $f_{\rm smin}$ and upper bound $f_{\rm smax}$. The optimal frequency is applied to the IPT system, and increased and decreased by a step change Δf for $f_{\rm s}[k+1]$. The initial frequency of MPFC $f_{\rm sini}$ is preliminarily determined based on the predictive (6) by setting $I_{\rm o}[k+1]=I_{\rm o}[k]=I_{\rm ref}$. The flowchart of the algorithm to determine $f_{\rm sini}$ is depicted, as shown in Fig. 8. Initially, the magnitude of the system transconductance $g_{\rm m}$ at the resonant frequency is calculated based on (17) and the frequency to achieve ZVS, i.e., $f_{\rm szvs}$, is calculated using

$$f_{\rm szvs}=\frac{\omega_{\rm o}}{2\pi}\sqrt{\frac{\left(2-\frac{1}{Q_{\rm s}^2}\right)+\sqrt{\frac{4M^2}{L_{\rm p}L_{\rm s}}-\frac{4}{Q_{\rm s}^2}+\frac{1}{Q_{\rm s}^4}}}{2\left(1-\frac{M^2}{L_{\rm p}L_{\rm s}}\right)}} \tag{19.1}$$

$$\text{s.t.}\ \frac{4M^2}{L_{\rm p}L_{\rm s}}-\frac{4}{Q_{\rm s}^2}+\frac{1}{Q_{\rm s}^4}>0 \tag{19.2}$$

where $Q_{\rm s}$ is the quality factor of the receiver resonator, which is calculated based on

$$Q_{\rm s}=\frac{\omega_{\rm o}L_{\rm s}}{R_{\rm s}+R_{\rm eqL}}\,. \tag{19.3}$$

The transconductance $g_{\rm m}$ is compared to $\frac{8I_{\rm ref}}{\pi^2V_{\rm in}}$. If $g_{\rm m}$ is greater than $\frac{8I_{\rm ref}}{\pi^2V_{\rm in}}$, the IPT system has two independent frequencies (i.e., $f_{\rm sini1}>f_{\rm sini2}$). Otherwise, the IPT system has four independent frequencies (i.e., $f_{\rm sini1}>f_{\rm sini2}>f_{\rm sini3}>f_{\rm sini4}$) [23]. The initial frequency $f_{\rm sini}$ is primarily assigned by $f_{\rm sini1}$ to ensure

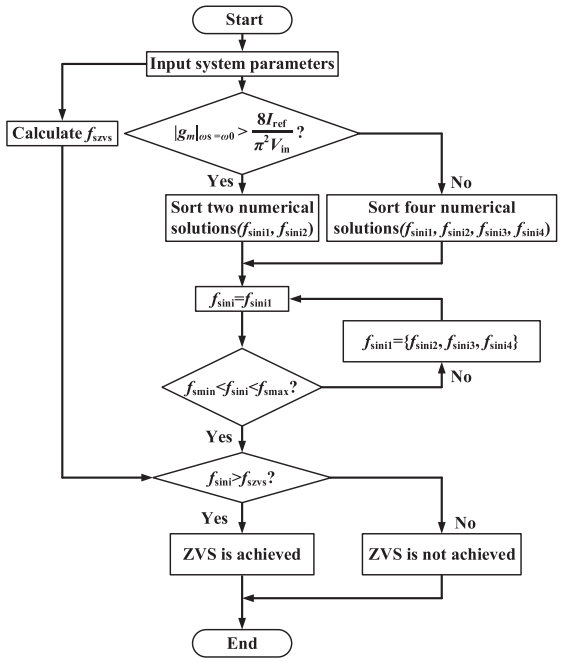

Fig. 8. Flowchart of the algorithm to determine $f_{\rm sini}$.

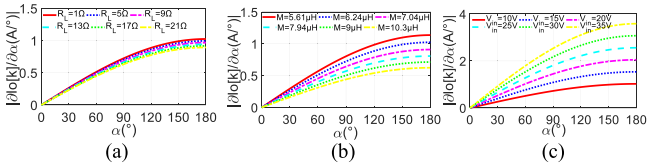

Fig. 9. Curves of $|\frac{\partial I_{\rm o}[k]}{\partial\alpha}|-\alpha$ for the IPT systems with (a) $M=6.243$ μH and $V_{\rm in}=10$ V, (b) $V_{\rm in}=10$ V and $R_{\rm L}=1$ Ω, and (c) $M=6.243$ μH and $R_{\rm L}=1$ Ω.

ZVS. However, $f_{\rm sini}$ is checked with the frequency boundaries. If $f_{\rm sini}$ is beyond the limits, $f_{\rm sini2}$ is assigned for $f_{\rm sini}$ (analogy for $f_{\rm sini3}$ and $f_{\rm sini4}$). Otherwise, $f_{\rm sini}$ is compared to $f_{\rm szvs}$ to indicate whether the IPT system can operate with ZVS or not.

Both MPPC and MPFC can be easily implemented using inexpensive digital controllers. However, the MPFC needs more computation to determine the initial frequency $f_{\rm sini}$, while is easier to achieve ZVS using more cost-effectives software methods.

VI. Simulation Results

To exhibit the sensitivities of the phase shift angle α on the output current $I_{\rm o}$, the relationship between $\left|\frac{\partial I_{\rm o}[k]}{\partial\alpha}\right|$ and α are plotted based on (9) and the parameters given in Table II, as shown in Fig. 9. The nominal mutual inductance M, input voltage $V_{\rm in}$, and load resistance $R_{\rm L}$ are set to be 6.243 μH, 10 V, and 1 Ω, respectively. Apparently, the sensitivities of $I_{\rm o}$ with respect to α decrease when $R_{\rm L}$ and M increase, while the sensitivities of $I_{\rm o}$ with respect to α decrease when $V_{\rm in}$ decreases, which validate the theoretical analyzes in Section III-A.

To verify the effects of the dead time of the transmitter-inverter on the MPPC, simulations are also conducted on the nominal

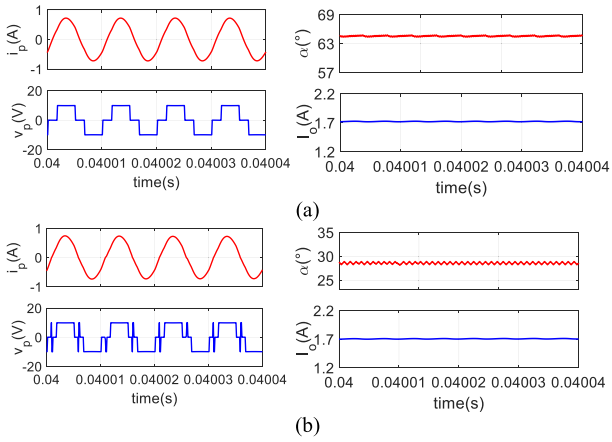

Fig. 10. Waveforms of $i_{\rm p}$, $v_{\rm p}$, α, and $I_{\rm o}$ for the nominal IPT system controlled by MPPC (a) without $T_{\rm d}$ and (b) with $T_{\rm d} = 1$ μs.

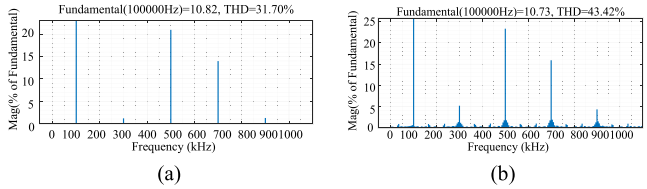

Fig. 11. FFT spectrums of $v_{\rm p}$ (a) without $T_{\rm d}$ and (b) with $T_{\rm d} = 1$ μs.

IPT system with the parameters given in Table II. $I_{\rm ref}$ is set to be 1.72 A. Fig. 10 shows the waveforms of $i_{\rm p}$, $v_{\rm p}$, α, and $I_{\rm o}$ for the system with and without settling a dead time. Without dead time (i.e., $T_{\rm d} = 0$ μs), α is controlled at 64.17° by the MPPC. On the other hand, α is controlled at 28.65° by settling $T_{\rm d} = 1$ μs and $\varphi_{T_{\rm d}} = 36°$ ($T_{\rm ond}$ is set to be identical to $T_{\rm offd}$). Obviously, $v_{\rm p}$ of the IPT system with $T_{\rm d} = 1$ μs has notching effects, while $v_{\rm p}$ of the IPT system with $T_{\rm d} = 0$ μs has no voltage-polarity reversal phenomenon. This validates the operation analyzes that the dead time effects of $v_{\rm p}$ are unavoidable for the MPPC when $\alpha < \varphi_{T_{\rm d}+T_{\rm ond}-T_{\rm offd}}$. The fast Fourier transform (FFT) spectrums of $v_{\rm p}$ are shown in Fig. 11. The total harmonic distortion (THD) of $v_{\rm p}$ with notching effects is 43.42%, which is much greater than 31.7% for the THD of $v_{\rm p}$ without notching effects. Besides, the controlled α is dwindled from 64.17° to 28.65° by settling the dead time. If α is controlled at 0° for a case without dead time, $I_{\rm o}$ cannot be regulated to track the same $I_{\rm ref}$ by settling the dead time. Therefore, the controllable output range of MPPC will be reduced.

Simulations are also carried out on the nominal IPT system controlled by MPFC with and without settling a dead time. The output current reference is 0.215 A. The initial frequency is calculated to be 120.1 kHz. The waveforms of $i_{\rm p}$, $v_{\rm p}$, α, and $I_{\rm o}$ for MPFC without the dead time (i.e., $T_{\rm d} = 0$ μs) and with the dead time (i.e., $T_{\rm d} = 1$ μs) are shown in Fig. 12. Both switching frequencies of the transmitter inverter are controlled at 119 kHz. Apparently, the dead time of MPFC will not affect the output control performance. Additionally, the other initial frequency can be calculated to be 85.8 kHz. The corresponding waveforms

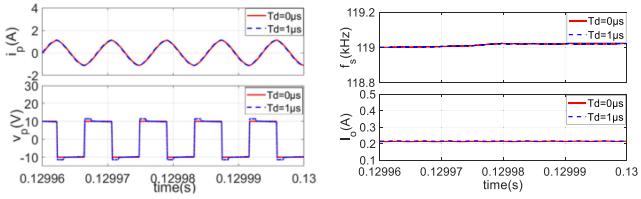

Fig. 12. Waveforms of $i_{\rm p}$, $v_{\rm p}$, α, and $I_{\rm o}$ for the nominal IPT system controlled by MPFC without $T_{\rm d}$ and with $T_{\rm d} = 1$ μs at $f_{\rm s} = 119$ kHz.

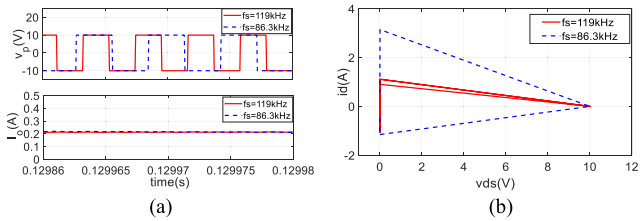

Fig. 13. Waveforms of (a) $v_{\rm p}$ and $I_{\rm o}$ for the nominal IPT system controlled by MPFC at 86.3 kHz, and (b) $v_{\rm ds}$-$i_{\rm d}$ curves of the transmitter inverter switches.

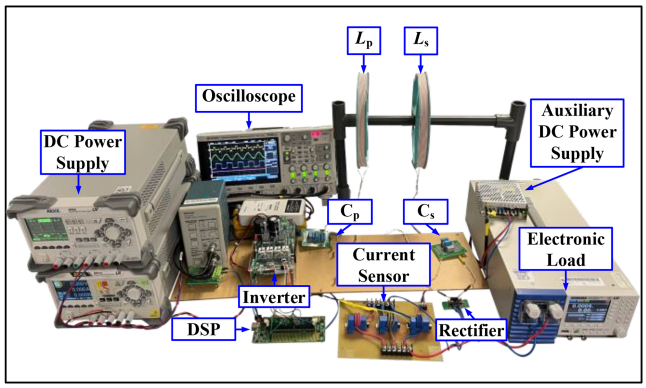

Fig. 14. Photograph of the experimental setup.

are shown in Fig. 13(a). The switching frequency of the transmitter inverter is controlled at 86.3 kHz. Although the output current can be well regulated to track the reference, the switching loss of $f_{\rm s} = 86.3$ kHz is greater than that of $f_{\rm s} = 119$ kHz, as can be seen from the $v_{\rm ds}$-$i_{\rm d}$ curves of the power switches in Fig. 13(b). This verifies the analysis that the IPT system with MPFC will have bifurcation phenomenon and the controller is better to be designed for the higher frequency above the resonant frequency to ensure ZVS.

VI. Experimental Verifications

Experiments are conducted on the prototype (as shown in Fig. 14) with the main parameters given in Table II. The nominal input voltage $V_{\rm in}$, mutual inductance M, and load resistance $R_{\rm L}$, are 15 V, 6.243 μH, and 1 Ω, respectively. $V_{\rm in}$ is implemented by RIGOL DP811A. $R_{\rm L}$ is emulated by an electronic load KIKUSUI PLZ405W. The transmitting and receiving coils, which are wound by 1.8 mm Litz wires with 11 turns, have the same diameter of 24 cm. The Schottky diodes SMC95SQ015

(i.e., $V_F = 0.26$V@25 °C, 2A) are used to form the diode-bridge rectifier. The hall sensor LEM25-P is adopted to feedback I_o to the digital signal processor (DSP) TMS320F28335 to drive the primary-side evaluation board TARAZ SPM-FB-SiC via a communication link. The timer interrupt time is fixed at 30 μs. The sampling frequencies of both MPPC and MPFC are fixed at 100 kHz. T_{ond} and T_{offd} of the inverter are 54 and 28 ns, respectively. The experimental waveforms are captured from the oscilloscope KEYSIGHT DSOX2004A.

A. Steady State and Dynamic Tracking Performance

To exhibit superior dynamic tracking performance of the proposed MPPC and MPFC over conventional PI-based phase shift control and PI-based frequency control, comparisons are given based on the IPT system with $V_{in} = 15$V and $M = 6.243$ μH. R_L is changed from 1 to 7 Ω for the first dynamics, while I_{ref} is changed from 0.84 to 1.68 A for the second dynamics. The dead time of MPPC is set to be $T_d = 0.1$ μs. The occupation time of conventional PI-based phase shift control, proposed MPPC, conventional PI-based frequency control, and proposed MPFC are 3, 21,11, and 28 μs, respectively. The initial frequency of MPFC is set to be $f_{init} = 112.6$ kHz based on (8). The step changes of the MPPF and MPFC are $\Delta\alpha = 0.018°$ and $\Delta f = 0.25$ Hz, respectively. The proportional and integral gains of the PI-based phase shift control and PI-based frequency control are optimally tuned to be 3/A and 0.000025/A, 1Hz/A and 0.0004Hz/A, respectively, for making sure that the settling time of the first dynamic change (i.e., 3 ms) are identical to those of MPPC and MPFC. The waveforms of v_p, i_p, I_o, and U_o are shown in Fig. 15. For PI-based phase shift control and MPPC, both α are controlled at 148°, 146°, and 110° at three steady states, respectively. For PI-based frequency control and MPFC, both f_s are controlled at 111.1, 108.7, and 102 kHz at three steady states, respectively. As a result, I_o can be well regulated to track I_{ref} with negligible offsets for all the four control methods. $I_{o\cdot AVG}$ and $U_{o\cdot AVG}$ are the average values of I_o and U_o. The overshoots of first dynamics (i.e., R_L is changed from 1 to 7 Ω) for both MPPC and MPFC are almost zero, while the overshoot of the PI-based phase shift control is 2 V and the overshoot of the PI-based frequency control is 5 V. Without changing any control parameters, the overshoots of the second dynamics (i.e., I_{ref} is changed from 0.84 to 1.68 A) for both MPPC and MPFC remain zero, while the overshoot of the PI-based phase shift control is 1 V and the overshoot of the PI-based frequency control is 3 V. The settling time of MPPC and MPFC are 35 and 34 ms, while those of the respective PI control are 61 and 60 ms. Obviously, the dynamic responses of MPPF and MPFC are significantly improved as compared to the PI-based counterparts.

B. Effects of Dead Time on MPPC and MPFC

To validate the analysis that the dead time of transmitter-side inverters can affect the MPPC, experiments are carried out on the IPT system with $V_{in} = 10$V, $M = 6.243$ μH, $R_L = 1\Omega$, and $I_{ref} = 1.72$A. The dead time T_d is set to be 0.5 μs. Fig. 16 shows the waveforms of v_{an}, v_{bn}, v_p, i_p, and I_o of MPPC without T_d and with T_d. The phase shift angle is controlled at 66° to track

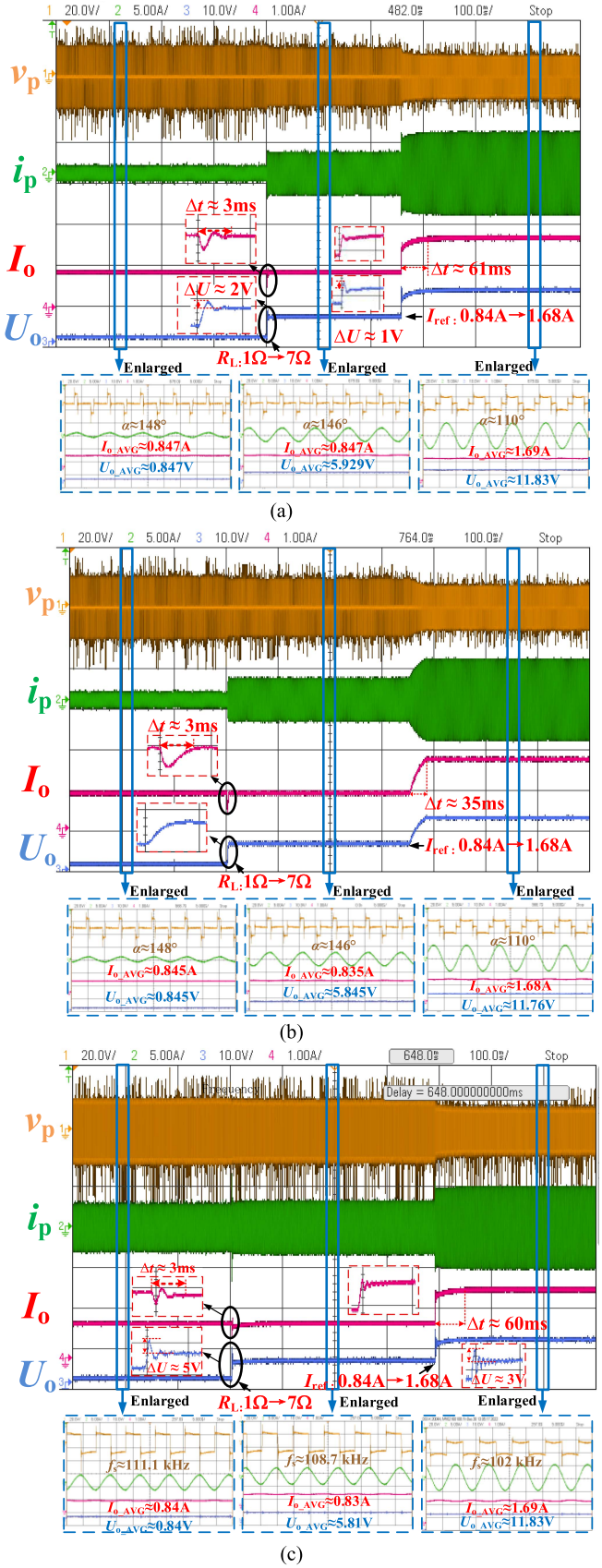

Fig. 15. Waveforms of v_p, i_p, I_o, and U_o for the IPT system controlled by (a) conventional PI-based phase shift control, (b) MPPC, (c) conventional PI-based frequency control.

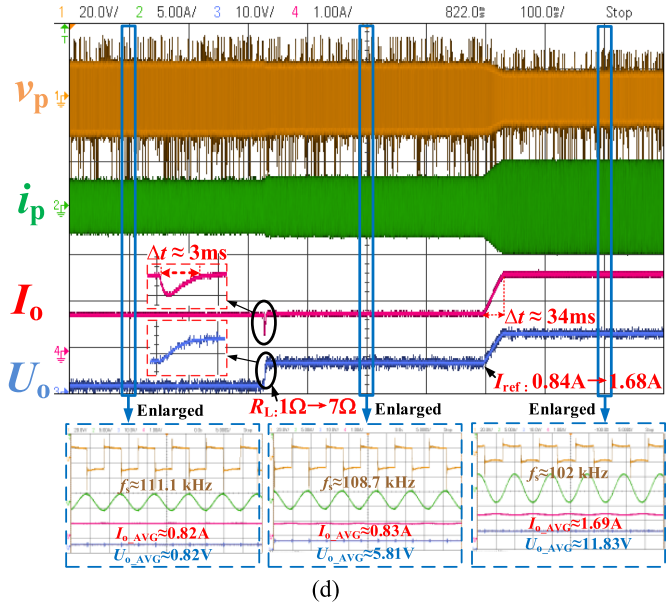

Fig. 15. *(Continued..)* Waveforms of v_p, i_p, I_o, and U_o for the IPT system controlled by (d) MPFC with R_L and I_{ref} changes.

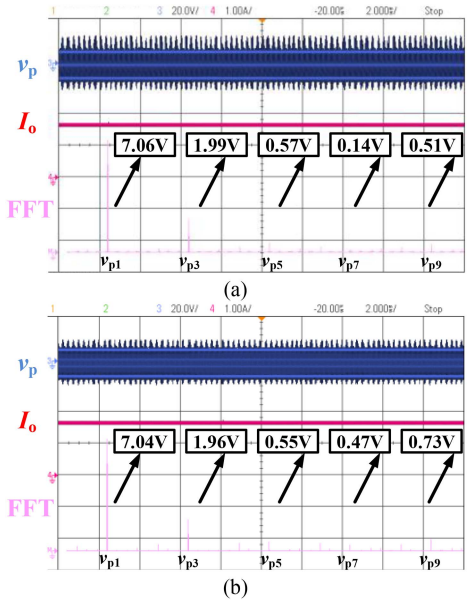

Fig. 17. FFT spectrums of v_p for the MPPC (a) without T_d and (b) with $T_d = 0.5$ μs.

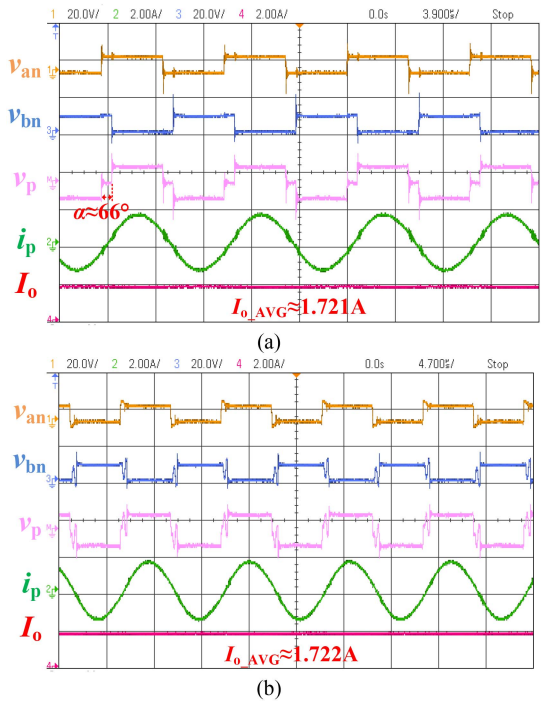

Fig. 16. Waveforms of v_{an}, v_{bn}, v_p, i_p, and I_o of MPPC (a) without T_d and (b) with $T_d = 0.5$ μs.

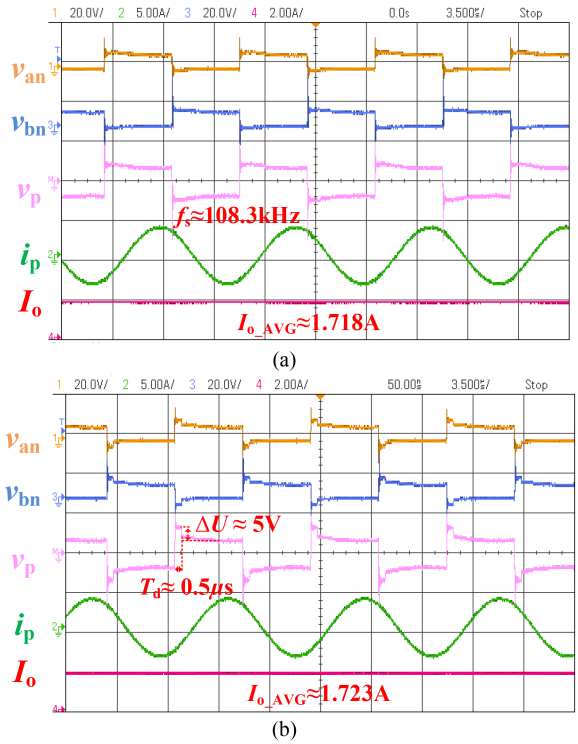

Fig. 18. Waveforms of v_{an}, v_{bn}, v_p, i_p, and I_o of MPFC (a) without T_d and (b) with $T_d = 0.5$ μs.

I_{ref} accurately. For MPPC with $T_d = 0.5$ μs, notching effects occur on v_p. The corresponding FFT spectrums of v_p are shown in Fig. 17. Apparently, the fundamental, third, and fifth-order harmonics (i.e., v_{p1}, v_{p3}, and v_{p5}) are almost the same, while the seventh and ninth-order harmonics (i.e., v_{p7} and v_{p9}) are increased from 0.14 to 0.47 V, and 0.51 to 0.73 V, respectively, by setting $T_d = 0.5$ μs. The THD of v_p for the MPPC with the dead time is 9.88%, while the THD is 9.16% for the MPPC without the dead time.

Experiments are also conducted on the same IPT system with MPFC. The waveforms of v_{an}, v_{bn}, v_p, i_p, and I_o are shown in Fig. 18. By controlling the frequency at 108.3 kHz, I_o is well regulated to track I_{ref} for both MPFC without T_d and MPFC with T_d. It is rational to set $T_d = 0.5$ μs for the adopted SiC-based inverter. The notching effects [observed in Fig. 16(b)] do not

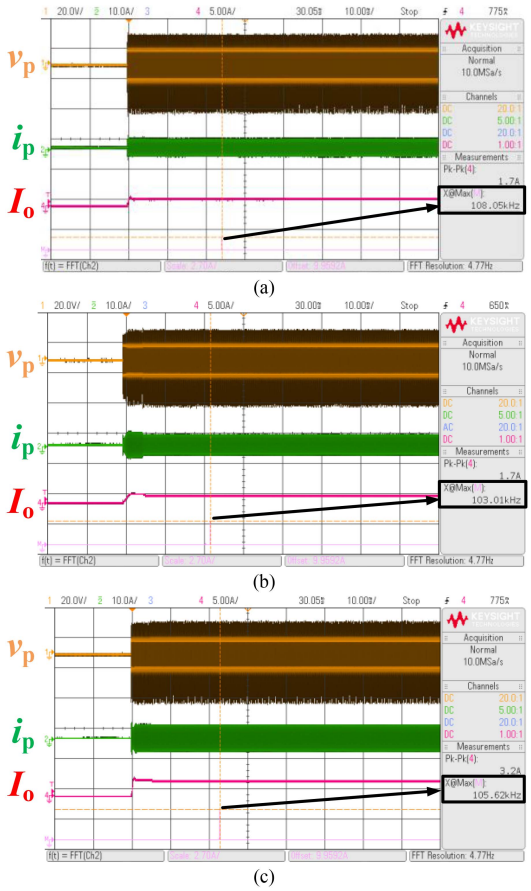

Fig. 19. Waveforms of v_p, i_p, and I_o of the IPT system with (a) $R_L = 1\ \Omega$ and $I_{ref} = 1.68$ A, (b) $R_L = 7\ \Omega$ and $I_{ref} = 1.68$ A, and (c) $R_L = 1\ \Omega$ and $I_{ref} = 3.2$ A controlled by MPFC.

occur for MPFC with T_d. The phase differences between v_p and i_p are the same for MPFC without T_d and MPFC with T_d (64° for both). The results verify the analysis that the dead time will affect MPPC but will not affect MPFC.

C. Determination of Initial Frequencies for MPFC

To demonstrate the effectiveness of the proposed algorithm (see Fig. 8) to determine proper initial frequencies of MPFC. Experiments are initially conducted on the IPT system with $V_{in} = 10$V, $M = 6.243\ \mu$H, $R_L = 1\Omega$, and $I_{ref} = 1.68$A. The frequency limits are $f_{smax} = 130$ kHz and $f_{smin} = 70$ kHz. Based on (8), the IPT system can operate at the frequencies $f_{sini1} = 108.7$ kHz, $f_{sini2} = 92.6$ kHz to track the reference. The magnitude of transconductance at the resonant frequency $|g_m|_{\omega s = \omega o}$ is calculated to be 0.2527 based on (17), which is greater than $\frac{8I_{ref}}{\pi^2 V_{in}}$. Thus, two numerical frequency solutions are sorted according to the algorithm. Since the maximum frequency f_{sini1} is within the frequency limits, it is compared to the ZVS frequency f_{szvs} which is calculated to be 105.4 kHz based on (19). Due to $f_{sini1} > f_{szvs}$, f_{sini1} can be finally adopted as the initial frequency for the MPFC. The practical waveforms of v_p, i_p, and I_o are shown in Fig. 19(a). The frequency of i_p is measured to be 108.05 kHz, which is very close to the calculated value.

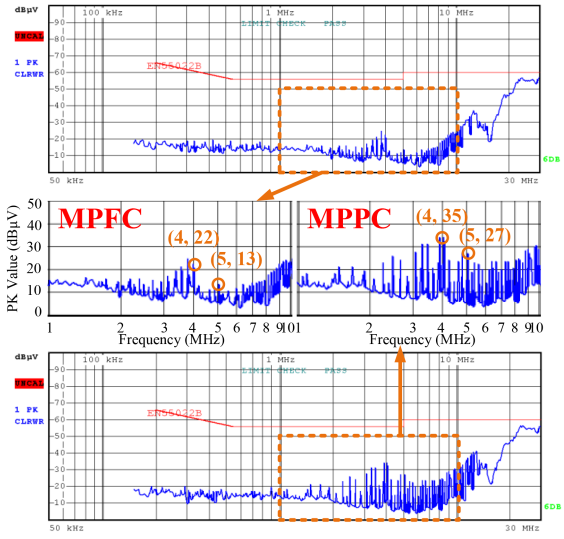

Fig. 20. Comparative EMI spectrums of the transmitter-side inverter controlled by MPPC and MPFC.

Besides, the output current (i.e., 1.7 A) is well-regulated to track the reference.

Then, R_L is changed from 1 to 7 Ω, while other parameters are kept the same. Based on (8), f_{sini1} and f_{sini2} are 105.6 kHz and 95.2 kHz, respectively. Based on (17), $|g_m|_{\omega s = \omega o}$ is calculated to be 0.2421, which is greater than $\frac{8I_{ref}}{\pi^2 V_{in}}$. The ZVS frequency f_{szvs} is 100 kHz. Thus, $f_{sini1} = 105.6$ kHz can be used as the initial frequency for the MPFC. The waveforms of v_p, i_p and I_o in Fig. 19(b) verify the effectiveness of the proposed algorithm (see Fig. 8) to lock the proper initial frequency and track the output current reference.

To further validate the generality of the proposed approach for an IPT system with four available frequencies to output the same I_o. Experiments are also conducted on the IPT system with $V_{in} = 10$V, $M = 6.243\ \mu$H, $R_L = 1\Omega$, and $I_{ref} = 3.2$A. The corresponding waveforms of v_p, i_p and I_o are shown in Fig. 19(c). The frequency of i_p is measured to be 105.62 kHz, and I_o is well-regulated to track the reference. For this case, the IPT system can operate at the frequencies $f_{sini1} = 107.4$ kHz, $f_{sini2} = 102.6$ kHz, $f_{sini3} = 97.7$ kHz, and $f_{sini4} = 93.8$ kHz to track the reference. The ZVS frequency f_{szvs} is calculated to be 105.4 kHz. Obviously, f_{sini1} is greater than f_{szvs}. Hence, f_{sini1} can be adopted as the initial frequency for the MPFC. The calculated f_{sini1} is close to the measured frequency of i_p, which proves the effectiveness of the proposed algorithm in Fig. 8.

D. EMI of Transmitter-Side Inverter With MPPC and MPFC

The EMI spectrums of the transmitter-side inverter being controlled by MPPC and MPFC are measured in ETS-Lindgren's Chamber Model 5405 GTEM! Test Cell. The comparative results are shown in Fig. 20. Although the peak values of radiation noise for the two control methods are less than the upper limit EN55022B, the peak values of MPFC are visibly less than those of MPPC within 1–10 MHz. The peak values of the radiation noise of MPFC are 22 dBμV@4 MHz and 13 dBμV@5 MHz,

while those of MPPC are 35 dBμV@4 MHz and 27 dBμV@5 MHz.

VII. Conclusion

This article compares two model predictive control (MPC) strategies, namely, MPPC and MPFC, for direct IPT systems. The two MPC approaches are newly designed for transmitter-side inverters based on the equivalent circuit models of typical direct IPT systems with only passive rectifiers and filters, and resistive loads at the receiver sides. Both control methods are empirically verified to have better dynamic performance than the PI-based counterparts at various operating conditions (except the nominal conditions). However, MPPC and MPFC have respective inherent drawbacks. Simulation and experimental results validate that the dead time of the transmitter inverter will affect MPPC to induce higher THD being caused by notching effects, and dwindle the control range under different operating conditions, while the dead time will not affect MPFC. The major issue of MPFC is to determine proper initial frequencies for IPT systems in achieving accurate output tracking and soft switching. In this article, a new algorithm is proved to be effective in finding out the optimal initial frequency by simulation and experimental results. The measured EMI of the transmitter-side inverter exhibits a better switching performance of the MPFC over the MPPC. Therefore, the proposed MPFC has an edge over the proposed MPPC for a direct IPT system if it is not required to operate at a fixed frequency.

References

[1] C. T. Rim and C. Mi, *Wireless Power Transfer For Electric Vehicles and Mobile Devices*. New York, NY, USA: Wiley, 2017.

[2] W. X. Zhong and S. Y. R. Hui, "Maximum energy efficiency tracking for wireless power transfer systems," *IEEE Trans. Power Electron.*, vol. 30, no. 7, pp. 4025–4034, Jul. 2015.

[3] H. Li, J. Li, K. Wang, W. Chen, and X. Yang, "A maximum efficiency point tracking control scheme for wireless power transfer systems using magnetic resonant coupling," *IEEE Trans. Power Electron.*, vol. 30, no. 7, pp. 3998–4008, Jul. 2015.

[4] Y. Jiang, L. Wang, J. Fang, C. Zhao, K. Wang, and Y. Wang, "A joint control with variable ZVS angles for dynamic efficiency optimization in wireless power transfer systems," *IEEE Trans. Power Electron.*, vol. 35, no. 10, pp. 11064–11081, Oct. 2020.

[5] Z. Huang, S.-C. Wong, and C. K. Tse, "An inductive-power-transfer converter with high efficiency throughout battery-charging process," *IEEE Trans. Power Electron.*, vol. 34, no. 10, pp. 10245–10255, Oct. 2019.

[6] M. Fu, H. Yin, X. Zhu, and C. Ma, "Analysis and tracking of optimal load in wireless power transfer systems," *IEEE Trans. Power Electron.*, vol. 30, no. 7, pp. 3952–3963, Jul. 2015.

[7] Y. Yang, W. Zhong, S. Kiratigongvoot, S. C. Tan, and S. Y. R. Hui, "Dynamic improvement of series-series compensated wireless power transfer systems using discrete sliding mode control," *IEEE Trans. Power Electron.*, vol. 33, no. 7, pp. 6351–6360, Jul. 2018.

[8] R. Mai, Y. Liu, Y. Li, P. Yue, G. Cao, and Z. He, "An active-rectified-based maximum efficiency tracking method using an additional measurement coil for wireless power transfer," *IEEE Trans. Power Electron.*, vol. 33, no. 1, pp. 716–728, Jan. 2018.

[9] R. Bosshard, J. W. Kolar, and B. Wunsch, "Control method for inductive power transfer with high partial-load efficiency and resonance tracking," in *Proc. Int. Power Electron. Conf.*, 2014, pp. 2167–2174.

[10] Y. Liu, U. Madawala, R. Mai, and Z. He, "An optimal multivariable control strategy for inductive power transfer systems to improve efficiency," *IEEE Trans. Power Electron.*, vol. 35, no. 9, pp. 8998–9010, Sep. 2020.

[11] W. Zhong and S. Y. R. Hui, "Charging time control of wireless power transfer systems without using mutual coupling information and wireless communication system," *IEEE Trans. Ind. Electron.*, vol. 64, no. 1, pp. 228–235, Jan. 2016.

[12] H. Liang, Y. Yang, and S. Y. R. Hui, "Improvement of Lithium-ion battery charging from the state-of-the-art Industrial JEITA Guidelines to a hybrid temperature-regulated current control," *IEEE Trans. Power Electron.*, vol. 37, no. 6, pp. 6412–6423, Jan. 2021.

[13] H. W. R. Liang, Y. Yang, L. He, J. Qu, C. K. Lee, and S. Y. R. Hui, "A multi-hysteresis control for minimizing battery charging time within industrial JEITA guidelines," *IEEE Trans. Ind. Electron.*, vol. 70, no. 8, pp. 8416–8425, Aug. 2023.

[14] Y. Jiang, L. Wang, Y. Wang, J. Liu, M. Wu, and G. Ning, "Analysis, design, and implementation of WPT system for EV's battery charging based on optimal operation frequency range," *IEEE Trans. Power Electron.*, vol. 34, no. 7, pp. 6890–6905, Jul. 2019.

[15] W. Liu, K. T. Chau, C. H. T. Lee, W. Han, X. Tian, and W. H. Lam, "Full-range soft-switching pulse frequency modulated wireless power transfer," *IEEE Trans. Power Electron.*, vol. 35, no. 6, pp. 6533–6547, Jun. 2020.

[16] K. Dang et al., "A 5.8-ghz high-power and high-efficiency rectifier circuit with lateral GaN schottky diode for wireless power transfer," *IEEE Trans. Power Electron.*, vol. 35, no. 3, pp. 2247–2252, Mar. 2020.

[17] S. Y. R. Hui, Y. Yang, and C. Zhang, "Wireless power transfer: A paradigm shift for the next generation," *IEEE J. Emerg. Sel. Topics Power Electron.*, vol. 11, no. 3, pp. 2412–2427, Jun. 2023.

[18] D. Thrimawithana and U. Madawala, "A primary side controller for inductive power transfer systems," in *Proc. IEEE Int. Conf. Ind. Technol.*, 2010, pp. 661–666.

[19] J. M. Miller, O. C. Onar, and M. Chinthavali, "Primary-side power flow control of wireless power transfer for electric vehicle charging," *IEEE J. Emerg. Sel. Topics Power Electron.*, vol. 3, no. 1, pp. 147–162, Mar. 2015.

[20] K. Yan, Q. Chen, J. Hou, X. Ren, and X. Ruan, "Self-oscillating contactless resonant converter with phase detection contactless current transformer," *IEEE Trans. Power Electron.*, vol. 29, no. 8, pp. 4438–4449, Aug. 2014.

[21] L. Xu, Q. Chen, X. Ren, S.-C. Wong, and C. K. Tse, "Self-oscillating resonant converter with contactless power transfer and integrated current sensing transformer," *IEEE Trans. Power Electron.*, vol. 32, no. 6, pp. 4839–4851, Jun. 2017.

[22] K. Wang and Y. Yang, "Advanced self-oscillating control for domino wireless power transfer systems with quasi-load-independent outputs," in *Proc. IEEE Energy Convers. Congr. Expo.*, 2022, pp. 1–7.

[23] T. Tan, K. Chen, Q. Lin, Y. Jiang, L. Yuan, and Z. Zhao, "Impedance shaping control strategy for wireless power transfer system based on dynamic small-signal analysis," *IEEE Trans. Circuits Syst. I: Regular Papers*, vol. 68, no. 3, pp. 1354–1365, Mar. 2021.

[24] P. Tan, H. He, and X. Gao, "Phase compensation, ZVS operation of wireless power transfer system based on SOGI-PLL," in *Proc. IEEE Appl. Power Electron. Conf. Expo.*, 2016, pp. 3185–3188.

[25] K. Inoue, K. Kusaka, and J.-I. Itoh, "Reduction in radiation noise level for inductive power transfer systems using spread spectrum techniques," *IEEE Trans. Power Electron.*, vol. 33, no. 4, pp. 3076–3085, Apr. 2018.

[26] Y. Yang and S. Y. R. Hui, "An augmented passive circuit for soft-switching of power inverter under phase-shift modulation control," New Technology Disclosure (NTU Ref: 2021-366; PolyU Ref: PAT-1416).

[27] Wireless power consortium website, Accessed: Jun. 23, 2022, [Online]. Available: https://www.wirelesspowerconsortium.com

[28] SAE International, "Wireless power transfer for light-duty plug-in/electric vehicles and alignment methodology," SAE J2954, Oct. 2020.

[29] AirFuel Alliance, Accessed: Jun. 23, 2022, Wireless charging technology & standards, [Online]. Available: https://airfuel.org

[30] Z. Li, H. Liu, Y. Tian, and Y. Liu, "Constant current/voltage charging for primary-side controlled wireless charging system without using dual-side communication," *IEEE Trans. Power Electron.*, vol. 36, no. 12, pp. 13562–13577, Dec. 2021.

[31] K. Song, Z. Li, J. Jiang, and C. Zhu, "Constant current/voltage charging operation for series–series and series–parallel compensated wireless power transfer systems employing primary-side controller," *IEEE Trans. Power Electron.*, vol. 33, no. 9, pp. 8065–8080, Sep. 2018.

[32] Q. Deng et al., "Multi-inverter phase-shifted control for IPT with overlapped transmitters," *IEEE Trans. Power Electron.*, vol. 36, no. 8, pp. 8799–8811, Aug. 2021.

[33] E. Gati, G. Kampitsis, I. Stavropoulos, S. Papathanassiou, and S. Manias, "Wireless phase-locked loop control for inductive power transfer systems," in *Proc. IEEE Appl. Power Electron. Conf. Expo.*, 2015, pp. 1601–1607.

[34] Y. Yao, Y. Yuan, Y. Wang, X. Liu, and D. Xu, "An efficient variable frequency control method for S/S-compensated wireless power transfer systems," in *Proc. IEEE 12th Energy Convers. Congr. Expo.-Asia*, 2021, pp. 1587–1592.
[35] R. P. Aquilera, P. Lezana, and D. E. Quevedo, "Finite-control-set model predicitve control with improved steady-state performance," *IEEE Trans. Ind. Inform.*, vol. 9, no. 2, pp. 658–667, May 2013.
[36] J. Rodríguez and P. Cortés, *Predictive Control of Power Converters and Electrical Drives*. Hoboken, NJ, USA: Wiley, 2012.
[37] Y. Yang, S.-C. Tan, and S. Y. R. Hui, "Adaptive reference model predictive control with improved performance for voltage-source inverters," *IEEE Trans. Control Syst. Technol.*, vol. 26, no. 2, pp. 724–731, Mar. 2018.
[38] J. M. González-González, A. Triviño-Cabrera, and J. A. Aguado, "Model predictive control to maximize the efficiency in EV wireless chargers," *IEEE Trans. Ind. Electron.*, vol. 69, no. 2, pp. 1244–1253, Feb. 2022.
[39] Z. Zhou, L. Zhang, Z. Liu, Q. Chen, R. Long, and H. Su, "Model predictive control for the receiving-side DC–DC converter of dynamic wireless power transfer," *IEEE Trans. Power Electron.*, vol. 35, no. 9, pp. 8985–8997, Sep. 2020.
[40] C. Qi, Z. Lang, L. Su, X. Chen, and H. Miao, "Finite-control-set model predictive control for a wireless power transfer system," in *Proc. IEEE Int. Symp. Predic. Control Elect. Drives Power Electron.*, 2019, pp. 1–5.
[41] S. Chen and W. Ding, "A novel finite-control-set model predictive voltage control for dynamic improvement of wireless power transfer systems," in *Proc. IEEE 4th Int. Elect. Energy Conf.*, 2021, pp. 1–6.
[42] Y. Yang, "Precise modeling of nonlinear rectifier loads in wireless power transfer systems," *IEEE J. Emerg. Sel. Topics Power Electron.*, vol. 11, no. 3, pp. 3574–3585, Jun. 2023.
[43] H. Xiao, Y. Yang, and K. Wang, "Dynamic improvement of direct inductive power transfer systems using adaptive model predictive-based phase shift control," in *Proc. IEEE Appl. Power Electron. Conf. Expo.*, 2023, pp. 2920–2925.
[44] U. D. Kavimandan, V. P. Galigekere, B. Ozpineci, O. Onar, and S. M. Mahajan, "The impact of inverter dead-time in single-phase wireless power transfer systems," *IEEE Trans. Power Electron.*, vol. 37, no. 1, pp. 1074–1089, Jan. 2022.
[45] K. Chen, K. W. E. Cheng, Y. Yang, and J. Pan, "A fast self-positioning-based optimal frequency control for inductive wireless power transfer systems without communication," *IEEE Trans. Ind. Electron.*, vol. 70, no. 1, pp. 334–343, Jan. 2023.

Huiwen Xiao received the B.Eng. degree in electrical engineering and automation from the Hebei University of Technology, Tianjin, China, in 2017, and the M.Eng. degree in electrical engineering from the University of Chinese Academy of Sciences, Beijing, China, in 2020. Since then, she was employed by the Institute of Electrical Engineering Chinese Academy of Sciences as an Engineer. From 2022 to 2023, she works as a Research Assistant at Hong Kong Polytechnic University. She will pursue her Ph.D. degree in electrical engineering from Hong Kong Polytechnic University since September 2023. Her research interests include wireless power transfer, power converters, and synchronous motor drives.

Yun Yang (Member, IEEE) received the B.Sc. degree from Wuhan University, Wuhan, China, in 2012, and the Ph.D. degree from the University of Hong Kong, Hong Kong, in 2017, both in electrical engineering.

He was a Research Assistant Professor with the Department of Electrical Engineering, The Hong Kong Polytechnic University, Hong Kong, from 2018 to 2020. He is currently an Assistant Professor with the School of Electrical and Electronic Engineering, Nanyang Technological University, Singapore. His research interests include wireless power transfer, renewable energy technologies, and power electronics.

Kaiyuan Wang (Student Member, IEEE) received the B.Eng. degree in electric engineering and automation from Northeast Electric Power University, Jilin, China, in 2020, the M.Sc. degree from The University of Hong Kong, Hong Kong, in 2021, and the M.Phil. degree from Hong Kong Polytechnic University, Hong Kong, in 2023, both in electrical engineering. He is currently working toward the Ph.D. degree in electrical engineering with Nanyang Technological University, Singapore.

His research interest includes wireless power transfer.

Jiayang Wu (Member, IEEE) received the B.Eng. degree in electrical information engineering from Zhejiang University, Hangzhou, China, in 2017, and the Ph.D. degree in electrical and electronic engineering from The University of Hong Kong, Hong Kong, in 2022.

She is currently a Research Fellow with the School of Electrical and Electronic Engineering, Nanyang Technological University, Singapore. Her current research interests include wireless power transfer, resonant converters, and renewable energy.

Dr. Wu was the recipient of the Best Paper Award (Second Place) of the IEEE TRANSACTIONS ON POWER ELECTRONICS in 2019. She also holds two Chinese patents and one U.S. patent.